

1                   **Climate impact of marine cloud brightening solar climate intervention under a**  
2                   **susceptibility based strategy simulated by CESM2**  
3

4   C.-C. Chen<sup>1</sup>, J. H. Richter<sup>1</sup>, Walker R. Lee<sup>1</sup>, Mari Tye<sup>1,2</sup>, Douglas G. MacMartin<sup>3</sup>, Ben Kravitz<sup>4,5</sup>

5       <sup>1</sup>Climate and Global Dynamics Division, NSF National Center for Atmospheric Research, Boulder, CO

6                   <sup>2</sup>Whiting School of Engineering, Johns Hopkins University, Baltimore, MD

7                                   <sup>3</sup>Cornell University

8                   <sup>4</sup>Department of Earth and Atmospheric Sciences, Indiana University, Bloomington, IN

9                   <sup>5</sup>Atmospheric Sciences and Global Change Division, Pacific Northwest National Laboratory,  
10                                   Richland, WA  
11

12   **Key Points:**  
13

- 14       • Susceptibility-based marine cloud brightening is simulated by a medium ensemble of
- 15       CESM2 simulations.
- 16       • Cloud seeding over 5% of the most easily brightened ocean surface is capable of
- 17       producing a net cooling of 1 °C.
- 18       • The 5% seeding strategy induces strong temperature and precipitation responses in lower
- 19       latitudes, resembling a La Niña-like pattern.

20   **Plain Language Summary:**

21   Marine cloud brightening, a form of solar climate intervention, could reflect some sunlight back  
22   to space and cool the planet. We used a state-of-the-art climate model to investigate what might  
23   happen if we target the regions of the ocean that are most easily brightened. Deploying marine  
24   cloud brightening over 5% of the ocean area can cool the planet by 1 °C in this model. However,  
25   it causes temperature and precipitation changes that look like La Niña. This may be undesirable  
26   for some people, meaning other marine cloud brightening strategies need to be investigated.

27  
28  
29   

---

  
30   Corresponding author: C.-C.Chen, [cchen@ucar.edu](mailto:cchen@ucar.edu)  
31  
32  
33  
34

## 35     **Abstract**

36             The efficiency of marine cloud brightening in cooling Earth's surface temperature is  
37 investigated by using a medium ensemble of simulations with the Community Earth System  
38 Model version 2 (CESM2). Various cloud seeding schemes based on susceptibility are examined  
39 to determine what area extent will be required to induce 1 °C cooling under SSP2-4.5. The results  
40 indicate that cloud seeding over 5% of the ocean area is capable of achieving this goal. Under this  
41 seeding scheme, cloud seeding is mainly deployed over lower latitudes where strong surface  
42 temperature and precipitation responses are induced. The simulations also reveal that the 5%  
43 cloud seeding scheme induces an overall reduction in global precipitation, with an increase over  
44 land and a decrease over the ocean.

## 146     **Introduction**

47             A number of solar climate intervention strategies have been proposed to counteract  
48 anthropogenic global warming. These strategies seek to enhance the albedo of the Earth and thus  
49 reflect more solar radiation back to space to induce a cooling effect. One strategy more  
50 extensively investigated is stratospheric aerosol injection (hereafter SAI) which attempts to  
51 mimic the cooling effect of large volcanic eruptions by injecting aerosols or their precursors into  
52 the stratosphere. Another less explored strategy seeks to brighten the marine boundary clouds by  
53 injecting sea salt particles to induce an increase in cloud drop number concentration [Latham,  
54 1990]. One of the reasons marine cloud brightening (hereafter MCB) is relatively less researched  
55 than SAI is due to the challenge of accurately simulating aerosol-cloud interactions in climate  
56 models (IPCC, 2021).

57             MCB aims to achieve a reduction in global surface temperature mainly by cloud indirect  
58 effects. By enhancing drop number concentration in clouds, cloud drops become smaller and thus  
59 clouds become more reflective of incoming solar radiation, known as the cloud albedo or  
60 Twomey effect [Twomey, 1974;Twomey, 1977]. As the cloud drop size is reduced, precipitation  
61 may be suppressed and the clouds become more persistent. This also leads to reflecting more  
62 solar radiation, known as the cloud lifetime or Albrecht effect [Albrecht, 1989].

63             There have been two main approaches in simulating a cloud seeding strategy for MCB  
64 intervention. The first approach assumes deployment of cloud seeding over fixed regions [Jones  
65 et al., 2009; Baugman et al., 2012]. The second seeks to maximize the cooling effects of cloud  
66 seeding by first searching for regions most susceptible to seeding and then constructing a seeding  
67 scheme accordingly [Latham et al., 2008;Rasch et al.,2009]. The first approach makes it a  
68 straightforward task to determine what causes the induced regional climate impact due to MCB

climate intervention. The advantage of the second approach, however, is its capability of inducing a maximum radiative effect with a minimum area extent to deploy cloud seeding.

Since MCB aims at enhancing cloud drop number concentration in boundary layer clouds, it is important for the model employed to be capable of accurately simulating cloud-aerosol interactions. For example, Wood [2021] demonstrated that the radiative forcing of MCB simulated by climate models could be highly sensitive to the assumption made in the aerosol activation parameterization. Alterskjær et al. [2013] found that injecting sea salt particles in certain sizes might lead to a warming effect instead of cooling; their simulations suggest that injection of sea salt in the Aitken mode could suppress the occurrence of supersaturation which led to reduction in activation of background aerosols, and consequently reduced the cloud drop number concentration. One method of obtaining the climate effects from MCB without aerosol microphysical parameterization uncertainties confounding the results is, instead of injecting sea salt particles in the model simulation, the cloud drop number concentrations for the boundary layer clouds within the designated seeding regions can be artificially increased. Latham et al. [2008] and Rasch et al. [2009] followed this approach; they used the Community Climate System Model version 3 (CCSM3) to conduct MCB simulations even though the model did not simulate cloud-aerosol interactions. More recently, Stjern et al. [2018] and Hirasawa et al. [2023] also conducted MCB simulations under this approach. Assuming sea salt particles of correct sizes are injected, the cloud drop number concentration can be enhanced to  $\sim 500/\text{cm}^3$  as shown in Alterskjær et al. [2013].

In this study, we present results from MCB simulations by the Community Earth System Model version 2 (CESM2), which has many updates from a much older generation of the model CCSM3 utilized in Latham et al. [2008] and Rasch et al. [2009]. Even though CESM2 is capable of simulating cloud-aerosol interactions, we will limit our investigation based on the constrained approach to reduce the uncertainty of the work resulting from the aerosol activation parameterization. We first identified regions most susceptible to cloud seeding following the methodology described in Latham et al, [2008] and Rasch et al. [2009] (also described in Section 2.3 below) to construct susceptibility-based seeding schemes. Then, we investigated the area extent required for cloud seeding to generate  $1^\circ\text{C}$  cooling relative to pre-industrial conditions. Finally, a 10-member ensemble under the seeding scheme capable of producing  $1^\circ\text{C}$  cooling was conducted, and we examined the climate impacts.

## **Methods**

### **2.1. Model description**

We use the Community Earth System Model version 2 (CESM2) [Danabasoglu et al., 2020] for all simulations in this study. This version was employed for the Coupled Model Intercomparison Project Phase 6 (CMIP6) [Eyring et al., 2016] in which CESM2 ranks highly among CMIP6 models in terms of simulating large-scale circulations and tropospheric climate over the historical time period [Simpson et al., 2020;Duviver et al., 2020;Coburn and Pruor, 2021].

CESM2 is a fully coupled Earth system model with prognostic atmosphere, land, ocean, sea-ice, and land-ice components. The atmosphere component, the Community Atmosphere Model version 6 (CAM6), uses a finite volume dynamical core with a  $1.25^{\circ} \times 0.9^{\circ}$  longitude-latitude mesh and 32 vertical levels with the model top at around 40 km. CAM6 uses the Zhang and McFarlane [1995] scheme for deep convection, the Cloud Layers Unified By Binormals (CLUBB) [Golaz et al., 2002;Larson, 2017] for shallow convection, boundary layer, and an updated version of Morrison-Gottelman microphysics scheme (MG2) [Gottelman and Morrison, 2015] for stratiform clouds and precipitation processes.

The ocean component remains the same as in CESM1 and is based on the Parallel Ocean Program version 2 (POP2) [Smith et al., 2010;Danabasoglu et al., 2012] with several advances. These include a new parameterization for mixing effects in estuaries, increased mesoscale eddy (isopycnal) diffusivities at depth, use of prognostic chlorophyll for shortwave absorption, use of salinity-dependent freezing-point together with sea-ice model, and a new Langmuir mixing parameterization in conjunction with the new wave model component [Danabasoglu et al., 2020]. POP2 operates on a mesh which is uniform in the zonal direction ( $1.125^{\circ}$ ) and varies significantly in the meridional direction with the finest resolution of  $0.27^{\circ}$  at the equator. In the Northern Hemisphere high latitudes, the finest/coarsest resolution is about  $0.38^{\circ}/0.64^{\circ}$  at the northwestern Atlantic Ocean/northwestern Pacific Ocean. In the Southern Hemisphere, the resolution monotonically changes to  $0.53^{\circ}$  at  $32^{\circ}\text{S}$  and remains constant further south. There are 60 vertical levels with a maximum depth of 5500 m with a uniform resolution of 10 m in the upper 160 m. CESM2 uses CICE version 5.1.2 (CICE5) [Hunke et al., 2015] as its sea-ice component and uses the same horizontal grid as POP2.

CESM2 uses the Community Land Model version 5 (CLM5) [Lawrence et al., 2019] with many updates from CLM4. CLM5 improves the model's hydrological and ecological realism and enhances the representation of anthropogenic land use activities on climate and carbon cycle [Danabasoglu et al., 2020]. The River Transport Model (RTM) used in CESM1 has been replaced with the Model for Scale Adaptive River transport (MOSART) [Li et al., 2013].

## **2.2. Reference simulations**

We assume the moderate Shared Socioeconomic Pathway scenario of SSP2-4.5 for this study. SSP2-4.5, a continuation of the Representative Concentration Pathway 4.5 (RCP4.5) scenario, is considered “middle of the road” and represents a medium range of future forcing pathways [O'Neill et al., 2016]. A 5-member reference ensemble with CESM2 under SSP2-4.5 was conducted for years 2015-2100 as part of the Coupled Model Intercomparison Project Phase 6 (CMIP6; Eyring et al., 2018). Surface temperature evolution and equilibrium climate sensitivity in these simulations are described in Meehl et al. [2020]. Since then, 5 additional ensemble members were carried out. Thus, a total of 10 ensemble members of CESM2 simulations under SSP2-4.5 are employed in this study. However, daily maximum and minimum temperatures were only archived for five members of the SSP2-4.5 ensemble [Richter et al., 2022]; statistical significance testing was therefore based on a bootstrap analysis to accommodate the reduced sample size.

## **2.3. Construction of seeding strategies**

In this study, we follow the methodology described in Latham et al. [2008] and Rasch et al. [2009] to employ a susceptibility-based strategy for cloud seeding. As aforementioned, the simulations are performed under a constrained approach, i.e. the cloud drop number concentration of low clouds within the boundary layer clouds over the designated seeding regions is prescribed to a predetermined value, set to  $375/\text{cm}^3$  below 850 hPa.  $375/\text{cm}^3$  is selected in this study because it was the more realistic number concentration assumed in Latham et al. [2008] and Rasch et al. [2009], as the higher assumed number concentration ( $1000/\text{cm}^3$ ) in these studies might not be achievable in reality (through personal conversation with Dr. Andrew Gettelman).

To determine susceptibility to cloud seeding for each grid cell over the ocean, two simulations under SSP2-4.5 between 2015 and 2034 are compared: one baseline run and the other with cloud seeding at every grid point over the ocean within the boundary layer clouds. Susceptibility is determined by the shortwave cloud forcing difference between the two simulations, i.e., if cloud seeding over a grid point induces stronger (more negative) shortwave cloud forcing (SWCF), it is considered more susceptible to seeding. Susceptibility of all grid points over the ocean is ranked based on shortwave cloud forcing differences. Seeding masks are built based on a designated percentage of the ocean area. As shown in Fig. 1, seeding masks ranging between 2.5% and 20% of the ocean surface are depicted. Since shortwave cloud forcing is the gauge for susceptibility, one factor that influences susceptible regions for cloud seeding is where incoming solar radiation is abundant. Another key factor in determining regions most susceptible to cloud seeding is the distribution of low clouds. As revealed in Fig. 1, during the boreal summer regions most susceptible to cloud seeding are mainly over the west coast of the US where stratocumulus is frequently present [Warren et al., 1998]. During the boreal winter, the most susceptible regions for cloud seeding shift to the southern hemisphere, mainly off the west coast of South America. These regions are over the eastern flank of an ocean gyre where persistent cloud decks are present. Fig. 2 shows the annual seeding masks. The results indicate that when cloud seeding is deployed over less than 5% of the ocean surface, regions most susceptible to seeding are mainly off the west coast of North and South America. When the seeding area expands, regions most susceptible to cloud seeding extend to the west coast of Australia and Africa. Nevertheless, it is important to note that even though the susceptibility-based cloud seeding strategy maximizes the radiative forcing by MCB intervention, it does not necessarily maximize the induced temperature effect.

The radiative forcing induced under the susceptibility-based seeding strategy simulated by CESM2 is depicted in Fig. 3a. Under the same methodology, Latham et al. [2008] showed a net negative shortwave cloud forcing of  $\sim 2.5 \text{ W/m}^2$  for seeding over 20% of the ocean area. Nevertheless, by CESM2 under SSP2-4.5, the net negative shortwave cloud forcing for the same amount of seeding is  $\sim 7.5 \text{ W/m}^2$ . The three fold difference can be explained by

the low cloud biases in the earlier model versions. As shown in Kay et al. [2012] there were strong negative low cloud biases in the Community Atmosphere Model version 4 (CAM4), most pronounced over the stratocumulus regions which are the ideal locations to deploy MCB. Since CAM4 is a model similar to what was used in Latham et al. [2008] and Rasch et al. [2009], it explains the much lower induced radiative forcing by MCB. With various updates in the physics of the model, CAM5 was found to significantly improve the representation of low clouds [Kay. et al., 2012]. Through personal conversation with Dr. Jen Kay, CAM6, the atmosphere component of CESM2, maintains the improvements in the representation of low clouds as found in CAM5. Consequently, MCB simulations carried out by CESM2 are much more credible due to its superior representation of low clouds compared with CCSM3 employed in Latham et al. [2008] and Rasch et al. [2009]. However, even with the significant improvement on the representation of low clouds in CAM5 over CAM4, CAM5 still maintains negative low cloud biases over the stratocumulus regions and thus the radiative forcing induced by MCB is likely to be underestimated within the current model framework.

It is worth noting that the radiative forcing at the tail portion of the ocean area is positive (Fig. 3a). Fig. 3b reveals that the incremental radiative forcing induced by seeding the top 15% of the ocean surface is very high. It becomes much lower until about 80%, and reverses signs beyond that. This is because this methodology is susceptibility-based and the grid points with positive SWCF differences induced by cloud seeding (a warming effect) will have the lowest rankings. Fig. 3b shows differential radiative forcing against percentage of the ocean area with cloud seeding.

## **Results**

### **3.1. Seeding strategy in meeting temperature targets**

In this study, we follow a similar experimental design to that outlined in Richter et al. [2022] for a 10-member ensemble of CESM2 simulations utilizing SAI in setting the climate target for the MCB ensemble simulations. Hence, we choose the main target to restore the global mean surface temperature ( $T_0$ ) between 2050 and 2069 to the 2020-2039 level under SSP2-4.5. The deployment of MCB is assumed to start in 2035. In addition to global average surface temperature ( $T_0$ ), Kravitz et al. [2017] proposed two extra temperature targets

which may be set for the purpose of climate intervention: 1) inter-hemispheric temperature gradient (T1), and 2) equator-to-pole temperature gradient (T2). T1 and T2 will also be assessed in the MCB ensemble, as in Richter et al. [2022].

To assess the area extent of cloud seeding required to meet the temperature target, we first conduct simulations under four seeding schemes: 2.5%, 5%, 7.5% and 12.5% of the ocean surface. The global mean surface temperature for these four simulations is illustrated in Fig. 4 which suggests that seeding over 5% of the ocean surface most closely reaches the T0 goal in the 2050 - 2069 average.

### 3.2. Ensemble MCB simulations

The first set of experiments suggest that seeding over 5% of the ocean surface is sufficient to meet the temperature target set in this study. We then proceed to conduct a 10-member ensemble simulations with the same seeding scheme. The ensemble simulations confirm that indeed cloud seeding over 5% of the ocean surface is what is needed to meet the temperature target set in this study (see Fig. 5a). Since here we only apply a constant seeding (and hence roughly constant forcing), the global mean surface temperature of the MCB ensemble is in a clear upward trend and exceeds the temperature target during the last 10 years of the simulations. In contrast, in the SAI simulations in Richter et al (2022) a feedback algorithm was used to adjust the injection rates annually to maintain a roughly constant global mean temperature.

Next, we examine the regional temperature response by the 5% MCB intervention. The impact on mean surface temperature by the 5% seeding scheme is illustrated by the difference between the 2050-2069 average under the MCB ensemble and the 2020-2039 average under the control ensemble (Figs. 6 a,d,g). The application of MCB results in intense regional surface temperature responses with magnitudes much stronger than the effect of climate change (compare Figs 6a,d,g with Figs. 6 c,f,i). The most pronounced cooling is found over the stratocumulus regions off the west coast of North and South America where cloud seeding is deployed regularly (see Fig. 2b), and cooling extends to the tropical West Pacific. Furthermore, it is found that the annual averaged surface temperature is lower over Alaska (Fig. 6a) which is mainly attributed to the stronger cooling during the boreal winter (Fig. 6c). The MCB ensemble simulations also reveal that over the Northwest Pacific, the Eastern US, the



Southern Ocean, and the Antarctic, the surface temperature is significantly warmer (Figs. 6 a,d,g) than the 2020-2039 average, indicating the MCB scheme employed is not able to restore the surface temperature in these regions back to the 2020-2039 level.

When using the 2050-2069 level from the control ensemble mean as the basis for comparison, the induced surface temperature response by MCB shows a different picture (Figs. 6 b,d,f). In such a comparison, lower surface temperature is found in a much broader area. Pronounced cooling over the main seeding regions, i.e. off the west coast of North and South America, is found in the annual mean (Fig. 6b) as well as during the boreal winter (Fig. 6d) and boreal summer (Fig. 6f). It is interesting to note that during the boreal winter even though seeding is mainly deployed in the Southern Hemisphere, strong cooling is present over the Arctic (Fig. 6d). Warmer surface temperature, however, is also present in the MCB ensemble mean, mainly over the Northwest Pacific and the South Pacific Convergence Zone (SPCZ). This reveals that under the MCB intervention, surface temperature becomes even warmer in these regions which will further intensify the warming effect by climate change. Thus, this is a highly undesirable outcome for such MCB intervention.

The pronounced cooler and warmer regions arising from the 5% seeding are further emphasized in the surface temperature extremes (annual hottest and coldest days and nights) illustrated in Fig. 7a,d,g,j. In contrast with SAI simulations [e.g. Richter et al., 2022; Tye et al., 2022], the greatest response is observed in the annual minimum daily minimum temperature (“Coldest Night”; Fig. 7j) while the least impact is apparent for the annual maximum daily maximum temperature (“Hottest Day”; Fig. 7b). Regions of particularly elevated temperature are primarily over land in the highest latitudes for the daily maximum temperatures (Figs. 7a,d), with increases up to 2K higher than those shown for surface mean temperature. Cooling of a similar magnitude is not as extensive, and only appears in the daily minimum temperatures (Figs. 7g,j).

Comparing the 2050-2069 level from the control ensemble mean to the annual temperature extremes under the MCB ensemble (Figs. 7b,e,h,k) also shows a different response than that of the surface mean temperature in Fig. 6. While the mean surface temperatures show decreases in temperature over most of the globe with comparison to climate change, only the hottest night (Fig. 7h) and

coldest night (Fig. 7k) show a similar universal cooling. In contrast, the coldest day (Fig. 7a) and hottest day (Fig. 7e) are cooler relative to climate change only over the areas of seeding; over land the temperatures are increased relative to climate change). As noted above, the differences in extreme temperature induced by climate change alone (the average between 2050 and 2069 against the average between 2020 and 2039, Figs. 7 c,f,i,l) is generally less than the differences with MCB. Increases are also greater in the higher latitudes (Kim et al. 2020), and by reason of their rarity only show statistical significance in regions where the changes, and also interannual variability, are small [e.g. Katz, 2010].

Next, we assess T1 and T2 under the MCB ensemble. The simulations indicate that the MCB ensemble cannot restore T1 and T2 between 2050 and 2069 to the 2020-2039 level. The MCB ensemble mean of T1 between 2050 and 2069 is lower than the average between 2020 and 2039 by the control ensemble, and higher for T2 (Figs. 5b,c). Different seeding strategies would be required to restore T1 and T2, assuming these are within the space of achievable objectives (Lee et al. 2020).

The annual precipitation response induced by MCB shows similar patterns by using either the 2020-2039 average or the 2050-2069 average of the control ensemble (Figs. 8 a,b) as the basis for comparison. The precipitation response is highly concentrated in the lower latitudes. Precipitation with MCB is seen to reduce over the Intertropical Convergence Zone (ITCZ) where colder surface temperature is induced by MCB, and the ITCZ slightly shifts northward as a strip of increased precipitation is present. Precipitation is also found to increase under MCB over the SPCZ, the maritime continent, Australia, and the Amazon. When broken down by convective and stratiform precipitation, it is found that both exhibit very similar patterns but the change in convective precipitation plays a more important role (Figs. 8c,d,e,f), which responds strongly to the surface temperature.

In comparison, the change in precipitation due to climate change is illustrated in Figs. 8c,f,i, which is in general much weaker in magnitude. The strongest difference is enhanced precipitation over the ITCZ (Fig. 8c), mainly due to convective precipitation (compare Figs. 8f,i). However, the magnitude of the change is still much weaker than that induced by the MCB intervention.

The precipitation response during the boreal winter and boreal summer is illustrated in Figs. 9 and 10. Similar to the annual precipitation response (Fig. 8), the most pronounced seasonal precipitation response is mainly found in the lower latitudes and exhibits similar features as the annual mean, e.g. decreased precipitation over the ITCZ, and increased precipitation over the SPCZ, the maritime continent, and Australia (see Figs. 9a,9b,10a,10b). However, such precipitation response is stronger in the boreal winter than in the boreal summer because the induced lower surface temperature by MCB over the tropical West Pacific is more pronounced during the boreal winter (compare Figs. 6d,g).

Differences in seasonal precipitation induced by MCB can be detected in several regions. Increased precipitation over the Northwest Pacific and the Amazon and decreased precipitation over the Northeast Pacific are only found during the boreal winter (compare Figs. 9a,9b,10a,10b). Since these features are also present in the annual mean (Figs. 8a,b), it is conceivable that such regional response is mainly attributed to the boreal winter. Finally, as previously observed in the annual mean, convective precipitation response is also stronger than stratiform precipitation in the seasonal average (compare Figs. 9c,d,e,f,10c,d,e,f).

The differing responses of convective and stratiform precipitation are reflected in the changes in the annual maximum daily precipitation total (“wettest day”, Fig. 11a). Increases in the wettest day are focused over the SPCZ and Australia, with a narrow increase over the Pacific Ocean aligned with a northward shift in the ITCZ. The largest decreases in the wettest day correlate with the colder regions over the main seeding region. The contrast between the simulations with and without MCB is accentuated for the most extreme precipitation, as it is for surface temperature extremes (Fig. 11b). While mean precipitation under unabated climate change shows distinctly wetter and drier regions, the wettest day increases everywhere (Fig. 11c).

Even though the surface temperature over the Northwest Pacific is warmer under the MCB ensemble annual mean (Figs. 6 a,d,g), precipitation is only increased in DJF (Fig. 9a) but not in JJA (Fig. 10a). The response in sea-level pressure over the North Pacific in DJF under the MCB ensemble (Fig. 12a) is in good agreement with the induced surface temperature change (Fig. 6d): the Aleutian low is weakened as surface temperature is cooler, and the sea-level pressure over the Northwest Pacific is lower as surface temperature is warmer. In

DJF, the warmer surface temperature over the Northwest Pacific enhances convective precipitation (Fig. 9d) and the lower sea-level pressure promotes stratiform precipitation (Fig. 9g). However in JJA, the warmer surface temperature over the Northwest Pacific leads to an increase in sea-level pressure (Fig. 12b). This suggests that the subtropical high (a warm core high) over the North Pacific extends over the west Pacific. The MCB ensemble average indicates that convective precipitation is increased (Fig. 10d), likely due to warmer surface temperature, but stratiform precipitation is decreased, likely due to subsidence induced by the subtropical high. Increases in convective precipitation are most likely to result in increases in the most extreme precipitation (Fig. 11a). These features imply that the MCB intervention is likely to influence the large-scale circulation over the North Pacific.

The MCB ensemble reveals that precipitation is increased over Amazon in DJF but not in JJA. This is likely due to the induced difference in total precipitable water. The MCB ensemble shows an increase in total precipitable water over the Northern Amazon in DJF (Fig. 12c), but the total precipitable water is decreased in JJA (Fig. 12d). The precipitation response over Amazon in DJF (Figs. 9a,d,g) shows a dipole structure, i.e., precipitation is increased in the north but is decreased in the south. Thus, the impact of the MCB intervention is to shift the precipitation over Amazon northward in DJF which is in good agreement with the change in total precipitable water.

Next, we examine the impact of the 5% ocean area seeding scheme on the globally averaged precipitation. As aforementioned, this seeding scheme is sufficient to restore T0 between 2050 and 2069 to the 2020-2039 level (Fig. 5a). Under this seeding scheme, the ensemble mean in global precipitation between 2050 and 2069 is lower than the 2020-2039 level (Fig. 13a). This result is consistent as Rasch et al. [2009] in which it was found that restoring precipitation required less area extent for cloud seeding than to restore T0; similar conclusions have been found for solar reduction (e.g., Bala et al 2008) and for SAI. The simulations also show that this seeding scheme induces lower precipitation over the ocean between 2050 and 2069 than the 2020-2039 level (Fig. 13b), but the precipitation over land between 2050 and 2069 is higher than the 2020-2039 level (Fig. 13c). As revealed in Fig. 8a, the increased precipitation over land is mainly found over Australia, India, and the maritime continent.

Next, we examine differences in radiative fluxes induced by the 5% MCB scheme. Longwave flux at the model top is in general reduced in the lower latitudes except in the equatorial region where longwave flux is increased (Fig. 14a). Lower longwave flux at the model top in the lower latitudes is consistent with lower surface temperature (Fig. 14q) which is a key factor in determining the upward longwave flux at the surface (Fig. 14h) based on the Stefan-Boltzmann law. The increase in longwave flux at the model top in the equatorial region is mainly attributed to cloud forcing (Fig. 14c). As shown in Fig. 8b, convective precipitation over the tropical Pacific is significantly reduced by the MCB intervention, which also results in reduction in mid and high clouds (Figs. 14n,o). Thus, less longwave radiation is absorbed by clouds in the equatorial region and thus higher longwave flux can reach the model top.

Induced response in all-sky shortwave flux at the model top by the MCB intervention (Fig. 14d) is dominated by cloud forcing (Fig. 14f). Shortwave flux at the model top is overall lower in the lower latitudes but is increased in the equatorial region. The lower shortwave flux at the model top in the lower latitudes is a direct response to the higher low cloud fraction (Fig. 14m) which reflects more shortwave radiation. Nevertheless, mid and high clouds in the equatorial region are reduced (Figs. 14n,o), likely due to suppression of convection by MCB intervention, and the total cloud fraction is lower (Fig. 14p), indicating the contribution from mid and high clouds more than offset the increase in low clouds. Thus less shortwave radiation is reflected which in turn increases shortwave flux at the model top (Fig. 14d) in the equatorial region.

It is interesting to note that both all-sky and clear-sky shortwave fluxes at the model top are increased over high latitudes in the southern hemisphere (Figs. 14d,e), which implies that less shortwave radiation is reflected. Since the difference in shortwave cloud forcing in this region is negative, i.e. more shortwave radiation is reflected by clouds, much less shortwave radiation is reflected by the surface. Due to negative shortwave cloud forcing differences in high latitudes over the southern hemisphere (Fig. 14f), less shortwave radiation is capable of reaching the surface (Fig. 14l). However, even less shortwave radiation is reflected by the surface in this region (Fig. 14k) which is due to loss of sea ice (Fig. 14r).

It is worth noting that the ensemble spread for sea ice in the northern hemisphere (Fig. 14r) is quite large even though the ensemble mean difference is near zero. This is potentially a reflection of a large ensemble spread in surface temperature difference (Fig. 14q). This indicates that the uncertainty for the prediction over the Arctic is quite high. In the southern hemisphere, however, the ensemble spread in sea ice is relatively smaller as well as the surface temperature. The ensemble simulations also suggest that the MCB intervention is incapable of restoring sea ice in the southern hemisphere between 2050 and 2069 to the 2020-2039 level (Fig. 14r).

Even though we have demonstrated through a 10-member ensemble simulations that cloud seeding over 5% of the ocean surface is capable of meeting the global average surface temperature goal, applying a steady forcing will not, of course, maintain a steady global average surface temperature, as shown in Fig. 5a. Maintaining a steady global average surface temperature would require that the seeding area be gradually increased.

The 5% MCB scheme induces cooling mostly confined in the lower latitudes. Furthermore, surface temperature becomes warmer under MCB intervention than the baseline ensemble average, mainly over the Northwest Pacific and the SPCZ (Figs. 6b,e,h), which is on top of warming due to climate change (Figs. 6c,f,i), and with greatest effect on the hottest days and nights (Figs. 7a,d,g). In order to eliminate such undesirable responses, it will require different MCB strategies than that examined in this study.

## **Conclusions**

In this study, we examine the efficiency of MCB climate intervention by CESM2 ensemble simulations. Compared with the previous study using CCSM3 [Latham et al., 2008, Rasch et al., 2009], it is found that MCB may induce a much greater impact with the same area extent of cloud seeding under CESM2. This is mainly due to the much more realistic representation of low clouds, especially stratocumulus, in CESM2 than CCSM3. Since cloud seeding aims to enhance the albedo of low clouds, it is thus essential to have good representation of low clouds in the model employed for MCB simulations.

We follow the methodology described in Latham et al. [2008] and Rasch et al. [2009] to build a seeding strategy based on susceptibility of cloud seeding over all oceanic model grid points. The advantage of this strategy is its capability to generate a maximum (negative) radiative

effect with minimum cloud seeding efforts. However, the disadvantage of this approach is the difficulty in interpreting the cause of certain regional climate impacts. If cloud seeding is assumed to occur over fixed regions, it will thus make it straightforward to interpret the cause of regional climate impact of MCB intervention. The downside of this approach, of course, is its lower efficiency to induce a cooling effect.

Under the protocol design in this study, it is found that cloud seeding over 5% of ocean surface is capable of restoring the global average surface temperature between 2050 and 2069 to the 2020-2039 level, under the SSP2.4-5 scenario. The 10-member ensemble of CESM2 simulations shows that MCB yields cooling mostly confined within lower latitudes. The most pronounced cooling in surface temperature occurs over where cloud seeding is regularly deployed, mainly off the west coast of North and South America, and cooling extends to the tropical west Pacific. As a result, MCB induces a La Nina-like response and shifts the ITCZ slightly northward. Furthermore, surface temperature over the Northwest Pacific and SPCZ under MCB intervention becomes warmer than the baseline ensemble mean (Fig. 6b) which indicates that the MCB intervention further intensifies warming due to climate change (Fig. 6c) over these regions. These features are highly undesirable outcomes delivered by the MCB intervention.

The MCB climate intervention is also found to induce a significant impact on precipitation. The most pronounced decrease in precipitation is *not* found over the places where MCB is deployed even though the direct impact of cloud seeding would lead to a decrease in precipitation due to the Albrecht effect. Instead, the strongest precipitation reduction is found over the ITCZ where lower sea surface temperature is induced by MCB. The simulations also reveal that reduction of convective precipitation plays a more important role in the total precipitation decrease. Even though the global average precipitation is reduced by MCB, it is found that precipitation is increased over land, mainly over Australia, the maritime continent, and the Amazon, with these regions also receiving considerable increases in the most extreme precipitation.

In the current study, we prescribe cloud drop number concentration in the designated cloud seeding regions instead of injecting sea salt particles. This bypasses the representation of aerosol activation processes which remain highly uncertain in climate models. While this constrained approach eliminates the uncertainty resulting from the model representation of aerosol activation, it also lacks the direct aerosol effect due to sea salt particle injections. In our future study we will investigate how deployment of MCB by injecting sea salt particles may impact the climate. Additionally, different seeding strategies will be explored which may simultaneously meet the temperature targets of T0, T1 and T2.

508

509 **Acknowledgements:**

510 The work is based upon work supported by the NOAA ERB grant NA22OAR4310481, and the  
511 NSF National Center for Atmospheric Research which is a major facility sponsored by the US  
512 National Science Foundation under Cooperative Agreement no. 1852977. The Community Earth  
513 System Model (CESM) project is supported primarily by the National Science Foundation.  
514 Computing and data storage resources, including the Cheyenne supercomputer  
515 (doi:10.5065/D6RX99HX), were provided by the Computational and Information Systems  
516 Laboratory (CISL) at NSF NCAR. Support for BK was provided in part by the Indiana University  
517 Environmental Resilience Institute. The Pacific Northwest National Laboratory is operated for the  
518 US Department of Energy by Battelle Memorial Institute under contract DE-AC05-76RL01830.

519

520 **Open Research**

521 **Data Availability Statement**

522 CESM tag cesm2.1.4-rc.08 was used to carry out the simulations and is also available at  
523 <https://doi.org/10.5281/zenodo.7271743> (CESM Team, 2022). CESM2 simulation output  
524 presented in this paper is available at <https://doi.org/10.5065/MRH9-B809>.

525

526 **References**

- 527 Albrecht, B. A.: Aerosols, Cloud Microphysics, and Fractional Cloudiness, *Science*, 245,  
528 1227–1230, <https://doi.org/10.1126/science.245.4923.1227>, 1989.
- 529 Alterskjær, K. and Kristjánsson, J. E.: The sign of the radiative forcing from marine cloud  
530 brightening depends on both particle size and injection amount, *Geophys. Res. Lett.*, 40,  
531 210–215, <https://doi.org/10.1029/2012GL054286>, 2013.
- 532 Baughman, E., Gnanadesikan, A., Degaetano, A., and Adcroft, A.: Investigation of the Surface  
533 and Circulation Impacts of Cloud-Brightening Geoengineering, *J. Climate*, 25,  
534 7527–7543, <https://doi.org/10.1175/JCLI-D-11-00282.1>, 2012.
- 535 Coburn, J. and Pryor, S. C.: Differential Credibility of Climate Modes in CMIP6, *J. Climate*, 34,  
536 8145–8164, 2021.
- 537 Danabasoglu, G., Bates, S. C., Briegleb, B. P., Jayne, S. R., Jochum, M., Large, W. G., Peacock,  
538 S., & Yeager, S. G. (2012). The CCSM4 ocean component. *Journal of Climate*, 25,  
539 1361–1389. <https://doi.org/10.1175/JCLI-D-11-00091.1>
- 540 Danabasoglu, G., Lamarque, J.-F., Bacmeister, J., Bailey, D. A., DuVivier, A. K., Edwards, J., et  
541 al. (2020). The Community Earth System Model Version 2 (CESM2). *Journal of*



542 *Advances in Modeling Earth Systems*, 12, e2019MS001916.  
 543 <https://doi.org/10.1029/2019MS001916>  
 544 DuVivier, A. K., Holland, M. M., Kay, J. E., Tilmes, S., Gettelman, A., and Bailey, D. A.: Arctic  
 545 and Antarctic sea ice mean state in the Community Earth System Model Version 2 and  
 546 the influence of atmospheric chemistry, *J. Geophys. Res.-Oceans*, 125, e2019JC015934,  
 547 <https://doi.org/10.1029/2019JC015934>, 2020.  
 548 Eyring, V., Bony, S., Meehl, G. A., Senior, C. A., Stevens, B., Stouffer, R. J., & Taylor, K. E.  
 549 (2016). Overview of the Coupled Model Intercomparison Project phase 6 (CMIP6)  
 550 experimental design and organization. *Geoscientific Model Development*, 9, 1937–1958.  
 551 <https://doi.org/10.5194/gmd-9-1937-2016>  
 552 Gettelman, A., & Morrison, H. (2015). Advanced two-moment bulk microphysics for global  
 553 models. Part I: Off-line tests and comparison with other schemes. *Journal of Climate*, 28,  
 554 1268–1287. <https://doi.org/10.1175/JCLI-D-14-00102.1>  
 555 Golaz, J.-C., Larson, V. E., & Cotton, W. R. (2002). A PDF-based model for boundary layer  
 556 clouds. Part I: Method and model description. *Journal of the Atmospheric Sciences*, 59,  
 557 3540–3551.  
 558 Hirasawa, H., Hingmire, D., Singh, H. A., Rasch, P. J., and Mitra, P. (2023) "Effect of Regional  
 559 Marine Cloud Brightening Interventions on Climate Tipping Elements" Geophysical  
 560 Research Letters, Accepted. Preprint DOI: 10.22541/essoar.168319813.32335439/v1  
 561 Hunke, E. C., Lipscomb, W. H., Turner, A. K., Jeffery, N., & Elliott, S. (2015). CICE: The Los  
 562 Alamos Sea Ice Model. Documentation and Software User's Manual. Version 5.1. *T-3*  
 563 *Fluid Dynamics Group*, Los Alamos National Laboratory, Tech. Rep. LA-CC-06-012.  
 564 Intergovernmental Panel on Climate Change (IPCC). *Climate Change 2021 – The Physical*  
 565 *Science Basis: Working Group I Contribution to the Sixth Assessment Report of the*  
 566 *Intergovernmental Panel on Climate Change*. Cambridge University Press; 2023.  
 567 Jones, A., Haywood, J., and Boucher, O.: Climate impacts of geoengineering marine  
 568 stratocumulus clouds, *J. Geophys. Res.*, 114, D10106,  
 569 <https://doi.org/10.1029/2008JD011450>, 2009.  
 570 Katz, Richard W. "Statistics of Extremes in Climate Change." *Climatic Change* 100, no. 1 (May  
 571 2010): 71–76. <https://doi.org/10.1007/s10584-010-9834-5>.  
 572 Kay, J. E., and Coauthors, 2012: Exposing Global Cloud Biases in the Community Atmosphere  
 573 Model (CAM) Using Satellite Observations and Their Corresponding Instrument  
 574 Simulators. *J. Climate*, **25**, 5190–5207, <https://doi.org/10.1175/JCLI-D-11-00469.1>.  
 575 Kim, Y.-H., S.-K. Min, X. Zhang, J. Sillmann, and M. Sandstad. "Evaluation of the CMIP6

Multi-Model Ensemble for Climate Extreme Indices.” *Weather and Climate Extremes* 29 (September 2020): 100269. <https://doi.org/10.1016/j.wace.2020.100269>.

Larson, V. E., (2017). CLUBB-SILHS: A parameterization of subgrid variability in the atmosphere. arXiv:1711.03675v2 [physics.ao-ph].

Latham, J.: Control of global warming?, *Nature*, 347, 339–340, <https://doi.org/10.1038/347339b0>, 1990.

Latham, J., Rasch, P., Chen, C.-C., Kettles, L., Gadian, A., Gettelman, A., Morrison, H., Bower, K., and Choullarton, T.: Global Temperature Stabilization via Controlled Albedo Enhancement of Low-Level Maritime Clouds, *Philos. T. R. Soc. A*, 366, 1882, 3969–3987, <https://doi.org/10.1098/rsta.2008.0137>, 2008.

Lawrence, D. M., Fisher, R. A., Koven, C. D., Oleson, K. W., Swenson, S. C., Bonan, G., Collier, N., Ghimire, B., van Kampenhout, L., Kennedy, D., Kluzek, E., Lawrence, P. J., Li, F., Li, H., Lombardozzi, D., Riley, W. J., Sacks, W. J., Shi, M., Vertenstein, M., Wieder, W. R., Xu, C., Ali, A. A., Badger, A. M., Bisht, G., Brunke, M. A., Burns, S. P., Buzan, J., Clark, M., Craig, A., Dahlin, K., Drewniak, B., Fisher, J. B., Flanner, M., Fox, A. M., Gentine, P., Hoffman, F., Keppel-Aleks, G., Knox, R., Kumar, S., Lenaerts, J., Leung, L. R., Lipscomb, W. H., Lu, Y., Pandey, A., Pelletier, J. D., Perket, J., Randerson, J. T., Ricciuto, D. M., Sanderson, B. M., Slater, A., Subin, Z. M., Tang, J., Thomas, R. Q., Val Martin, M., & Zeng, X. (2019). The Community Land Model Version 5: Description of new features, benchmarking, and impact of forcing uncertainty. *Journal of Advances in Modeling Earth Systems*, 11, 4245–4287. <https://doi.org/10.1029/2018MS001583>

Lee, W., MacMartin, D., Visionsi, D., and Kravitz, B.: Expanding the design space of stratospheric aerosol geoengineering to include precipitation-based objectives and explore trade-offs, *Earth Syst. Dynam.*, 11, 1051–1072, <https://doi.org/10.5194/esd-11-1051-2020>, 2020.

Li, F., Levis, S., & Ward, D. S. (2013). Quantifying the role of fire in the Earth system—Part 1: Improved global fire modeling in the Community Earth System Model (CESM1). *Biogeosciences*, 10, 2293–2314. <https://doi.org/10.5194/bg-10-2293-2013>

Meehl, G. A., Arblaster, J. M., Bates, S., Richter, J. H., Tebaldi, C., Gettelman, A., Medeiros, B., Bacmeister, J., DeRepentigny, P., Rosenbloom, N., Shields, C., Hu, A., Teng, H., Mills, M. J., and Strand, G.: Characteristics of future warmer base states in CESM2, *Earth Space Sci.*, 7, e2020EA001296, <https://doi.org/10.1029/2020EA001296>, 2020.

O'Neill, B. C., Tebaldi, C., van Vuuren, D. P., Eyring, V., Friedlingstein, P., Hurtt, G., Knutti, R., Kriegler, E., Lamarque, J.-F., Lowe, J., Meehl, G. A., Moss, R., Riahi, K., and

Sanderson, B. M.: The Scenario Model Intercomparison Project (ScenarioMIP) for  
 CMIP6, *Geosci. Model Dev.*, 9, 3461–3482, <https://doi.org/10.5194/gmd-9-3461-2016>,  
 2016.

Rasch, P. J., Latham, J., and Chen, C.-C.: Geoengineering by Cloud Seeding: Influence on Sea  
 Ice and Climate System, *Environ. Res. Lett.*, 4, 045112,  
<https://doi.org/10.1088/1748-9326/4/4/045112>, 2009.

Richter, J. H., Visioni, D., MacMartin, D. G., Bailey, D. A., Rosenbloom, N., Dobbins, B., Lee,  
 W. R., Tye, M., and Lamarque, J.-F.: Assessing Responses and Impacts of Solar climate  
 intervention on the Earth system with stratospheric aerosol injection (ARISE-SAI):  
 protocol and initial results from the first simulations, *Geosci. Model Dev.*, 15, 8221–  
 8243, <https://doi.org/10.5194/gmd-15-8221-2022>, 2022.

Simpson, I. R., Bacmeister, J., Neale, R. B., Hannay, C., Gettelman, A., Garcia, R. R., et al.  
 (2020). An evaluation of the large-scale atmospheric circulation and its variability in  
 CESM2 and other CMIP models. *Journal of Geophysical Research: Atmospheres*, 125,  
 e2020JD032835. <https://doi.org/10.1029/2020JD032835>

Smith, R., P. Jones, B. Briegleb, F. Bryan, G. Danabasoglu, J. Dennis, J. Dukowicz, C. Eden, B.  
 Fox-Kemper, P. Gent, M. Hecht, S. Jayne, M. Jochum, W. Large, K. Lindsay, M.  
 Maltrud, N. Norton, S. Peacock, M. Vertenstein, & S. Yeager (2010). The Parallel Ocean  
 Program (POP) reference manual, Ocean component of the Community Climate System  
 Model (CCSM), LANL Tech. Report, LAUR-10-01853, 141 pp.

Stjern, C. W., Muri, H., Ahlm, L., Boucher, O., Cole, J. N. S., Ji, D., Jones, A., Haywood, J.,  
 Kravitz, B., Lenton, A., Moore, J. C., Niemeier, U., Phipps, S. J., Schmidt, H., Watanabe,  
 S., and Kristjánsson, J. E.: Response to marine cloud brightening in a multi-model  
 ensemble, *Atmos. Chem. Phys.*, 18, 621–634, <https://doi.org/10.5194/acp-18-621-2018>,  
 2018.

Twomey, S.: Pollution and the planetary albedo, *Atmos. Environ.*, 8, 1251–1256, 1974.

Twomey, S.: The Influence of Pollution on the Shortwave Albedo of Clouds, *J. Atmos. Sci.*, 34,  
 1149–1152, [https://doi.org/10.1175/1520-0469\(1977\)034<1149:TIOPOT>2.0.CO;2](https://doi.org/10.1175/1520-0469(1977)034<1149:TIOPOT>2.0.CO;2),  
 1977.

Tye, M. R., K. Dagon, M. J. Molina, J. H. Richter, D. Visioni, B. Kravitz, and S. Tilmes. “Indices  
 of Extremes: Geographic Patterns of Change in Extremes and Associated Vegetation  
 Impacts under Climate Intervention.” *Earth System Dynamics* 13 (2022): 1233–57.  
<https://doi.org/10.5194/esd-13-1233-2022>.

Warren, S G, Hahn, C J, London, J, Chervin, R M, Jenne, R L, Colorado Univ., Boulder, CO,

644 Colorado Univ., Boulder, CO, and National Center for Atmospheric Research, Boulder,  
645 CO. *Global distribution of total cloud cover and cloud type amounts over the ocean*.  
646 United States: N. p., 1988. Web. doi:10.2172/5415329.

647 Wood, R.: Assessing the potential efficacy of marine cloud brightening for cooling Earth using a  
648 simple heuristic model, *Atmos. Chem. Phys.*, 21, 14507–14533,  
649 <https://doi.org/10.5194/acp-21-14507-2021>, 2021.

650 Zhang, G. J., & McFarlane, N. A. (1995). Sensitivity of climate simulations to the  
651 parameterization of cumulus convection in the Canadian climate center general-  
652 circulation model. *Atmosphere-Ocean*, 33(3), 407–446

653  
654  
655  
656  
657  
658  
659  
660  
661  
662  
663  
664  
665

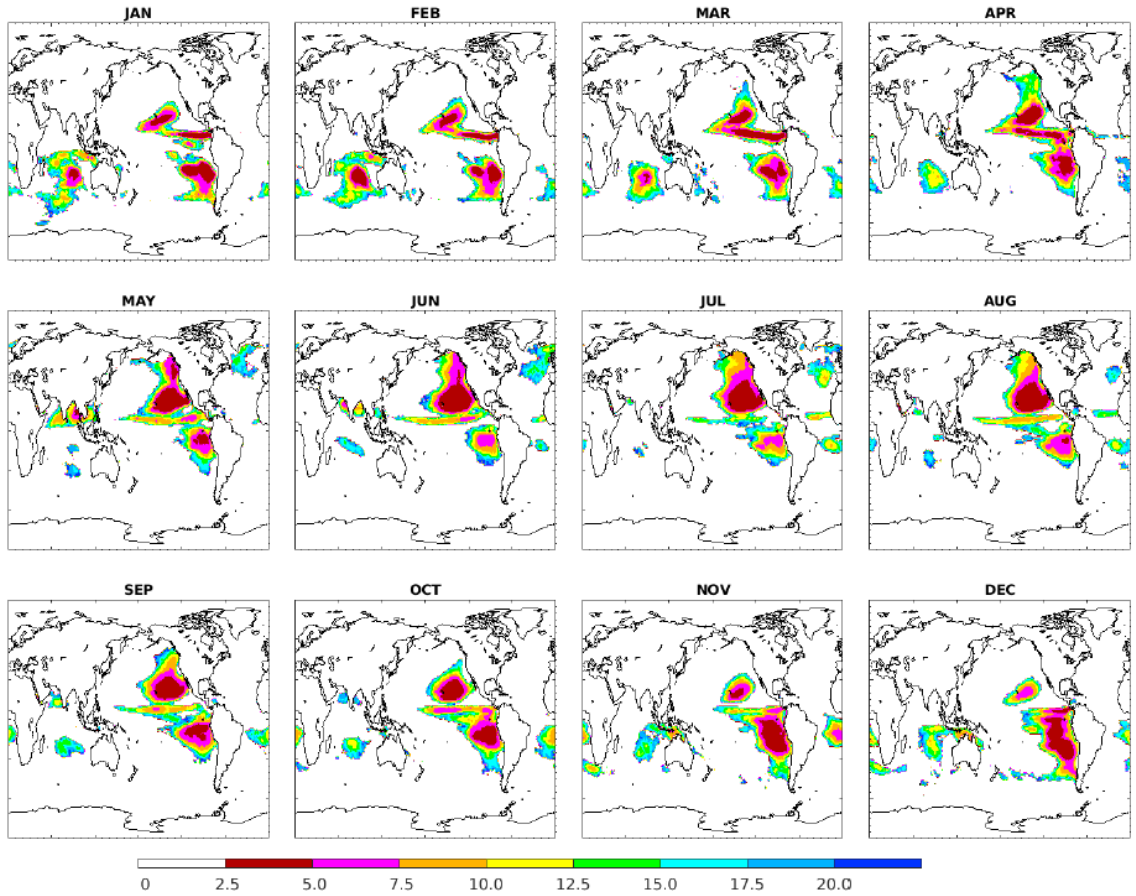
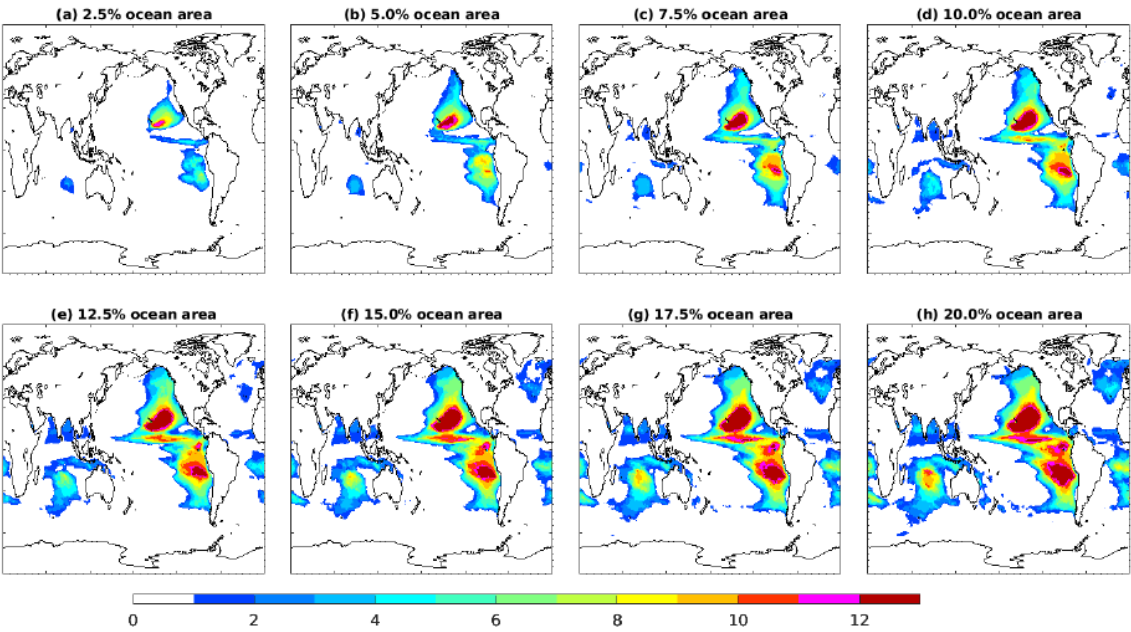


**Figure 1:** Monthly seeding masks based on the optimal seeding approach by using CESM2 simulations between 2015 and 2034 under SSP2-4.5 at 2.5% to 20% of the ocean area.

683



684

685

686

687

688

689

690

691

692

693

694

**Figure 2:** As in Fig. 1, but for the annually accumulated seeding masks. 1 means cloud seeding takes place in one month, and 12 means cloud seeding takes place all 12 months.

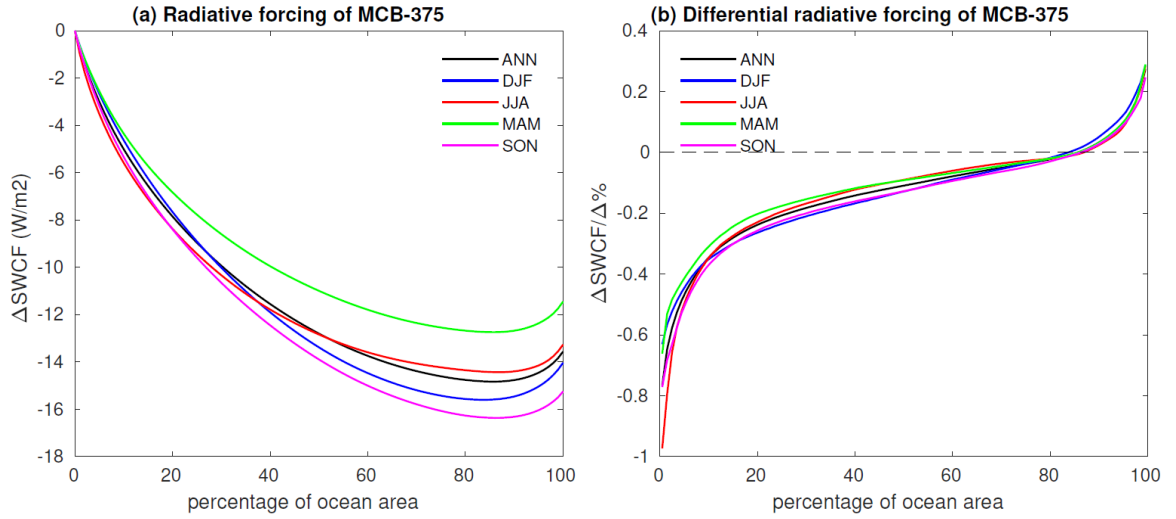


**Figure 3:** (a) Shortwave cloud forcing computed based on cloud seeding over all grid points over the ocean by using simulations between 2015 and 2034 under SSP2-4.5 as a function of areal extent for cloud seeding with a prescribed drop number concentration of  $375/\text{cm}^3$ , (b) differential shortwave cloud forcing based on the percentage of the ocean surface with cloud seeding. Annual (ANN) and seasonal (DJF, JJA, MAM, SON) averages are plotted.

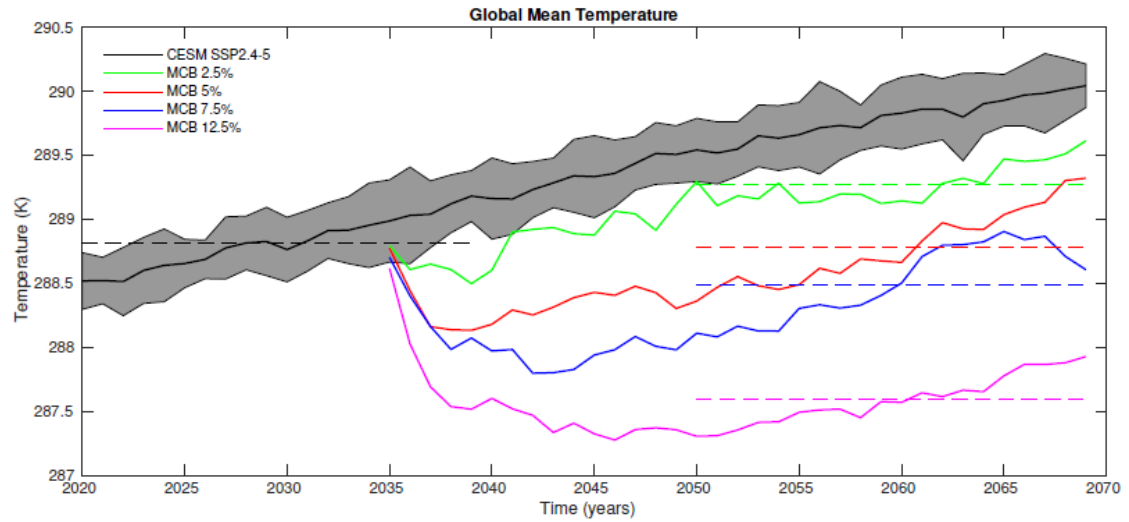
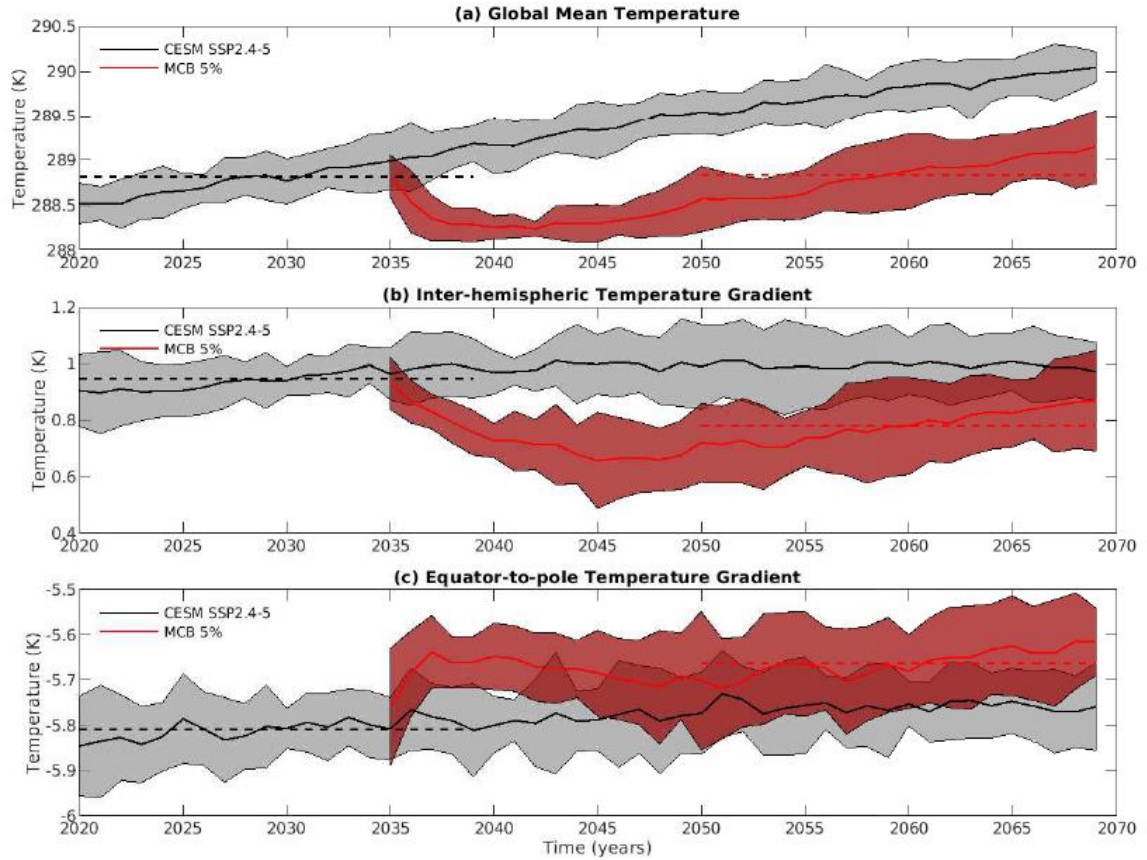


**Figure 4:** Time series of global average temperature. Black solid line represents the 10-member ensemble mean of the CESM2 simulations under SSP2-4.5, and the ensemble spread is two standard deviations of the ensemble. The black dashed line is the average between 2020 and 2039. The four colored solid lines represent MCB simulations over: 1) 2.5% (green), 2) 5% (red), 3) 7.5% (blue), and 4) 12.5% (magenta) of the ocean surface, and the dashed colored lines are averages between 2050 and 2069.



740  
741  
742  
743  
744



745  
746 **Figure 5:** Time series of a) global mean temperature ( $T_0$ ), b) inter-hemispheric temperature  
747 gradient ( $T_1$ ), and c) equator-to-pole temperature gradient ( $T_2$ ). Black and red solid lines  
748 represent the 10-member ensemble mean of the control and MCB (over 5% ocean surface)  
749 simulations with an ensemble spread of two standard deviations. The black dashed line is the  
750 average between 2020 and 2039, and the red dashed line is the average between 2050 and 2069.

751  
752  
753

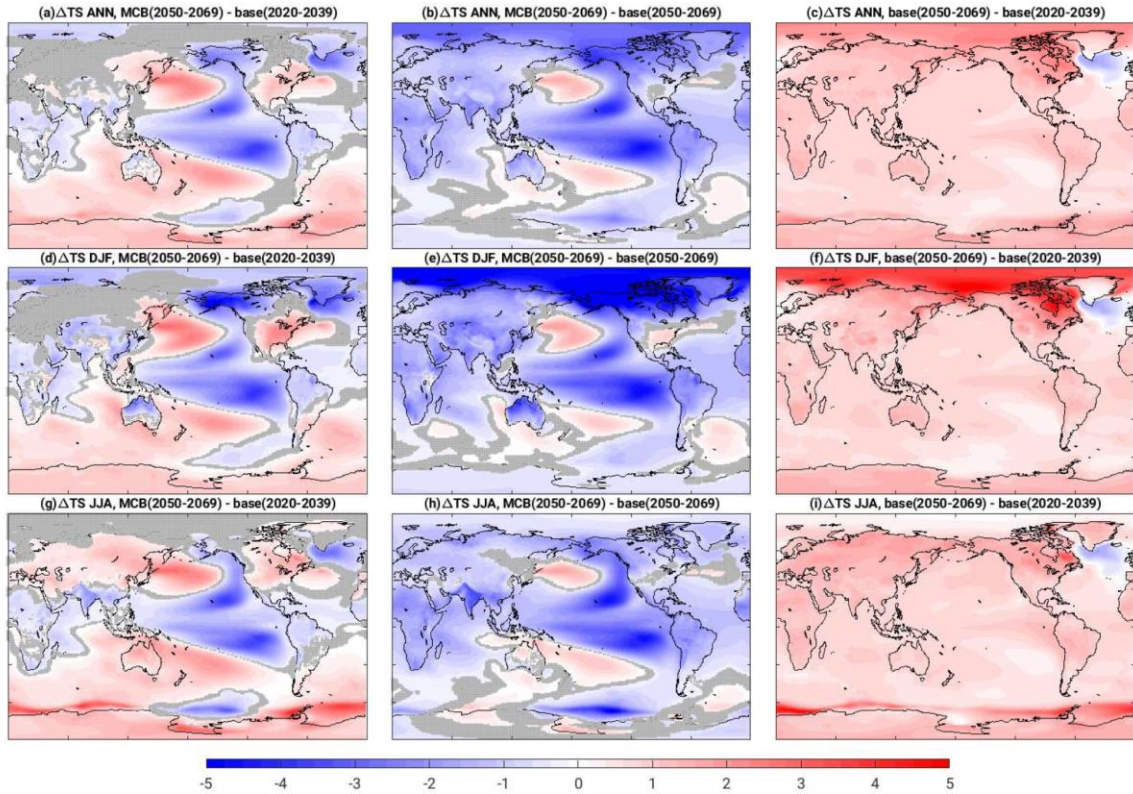


**Figure 6:** Difference in surface temperature (TS) in K between: 1) the ensemble mean of MCB over 5% ocean surface between 2050 and 2069 against the control ensemble mean between 2020 and 2039 (a,d,g), 2) the ensemble mean of MCB over 5% ocean surface between 2050 and 2069 against the control ensemble mean between 2050 and 2069 (b,e,h), and 3) the ensemble mean of the baseline model between 2050 and 2069 against the ensemble mean of the baseline model between 2020 and 2039 (c,f,i). Top panels are for annual average (ANN), middle panels are for the boreal winter average (DJF), and the bottom panels are for the boreal summer average (JJA). Differences under the 95% significance level are marked in gray dots.



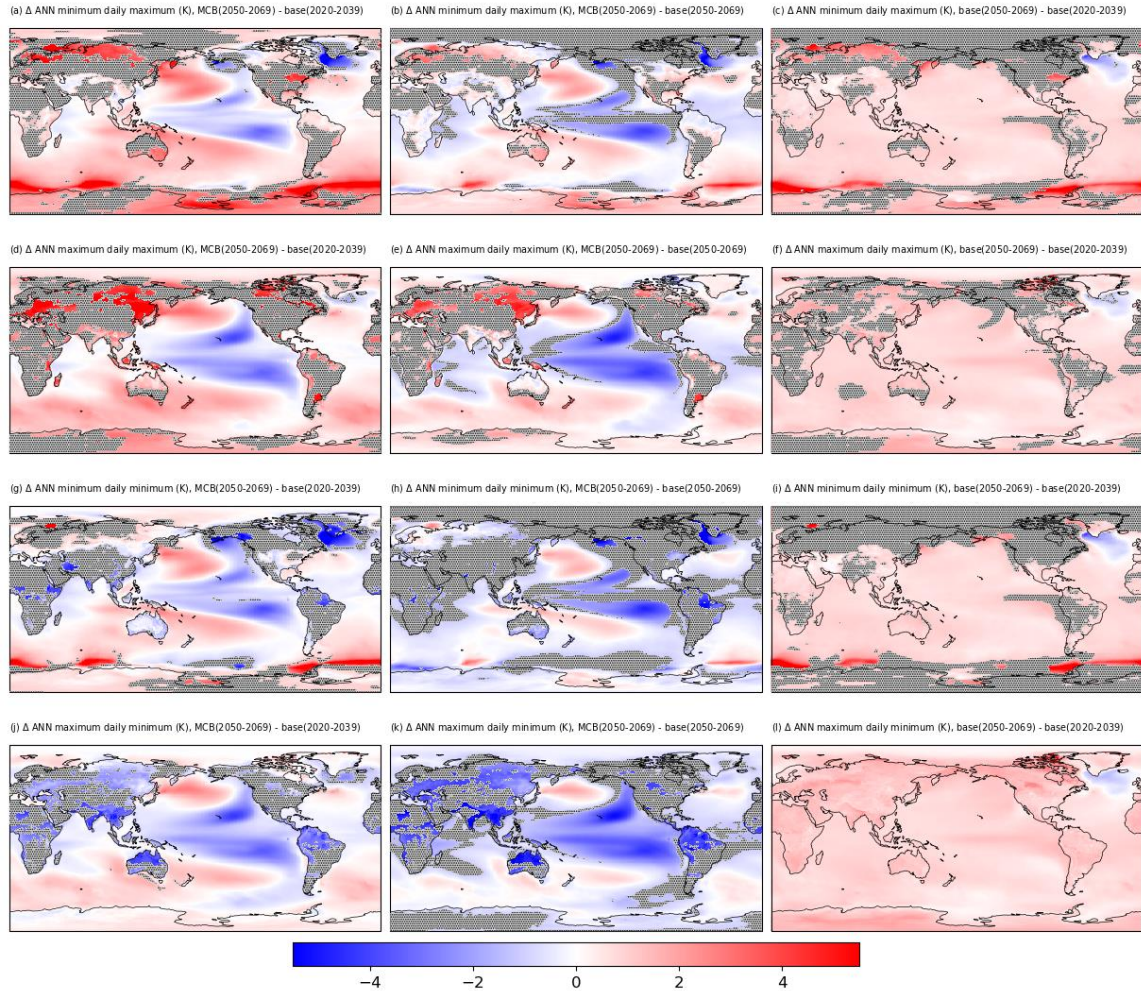


**Figure 7:** Difference in surface temperature between 1) the ensemble mean of MCB over 5% ocean surface between 2050 and 2069 against the control ensemble mean between 2020 and 2039 (a,d,g,j), 2) the ensemble mean of MCB over 5% ocean surface between 2050 and 2069 against the control ensemble mean between 2050 and 2069 (b,e,h,k), and 3) the ensemble mean of the baseline model between 2050 and 2069 against the ensemble mean of the baseline model between 2020 and 2039 (c,f,i,l). Row 1 is for annual minimum daily maximum (“Coldest Day”), row 2 is for annual maximum daily maximum (“Hottest Day”), row 3 is for annual minimum daily minimum (“Coldest Night”), row 4 is for annual maximum daily minimum (“Hottest Night”). Differences under the 95% significance level are marked in gray dots.

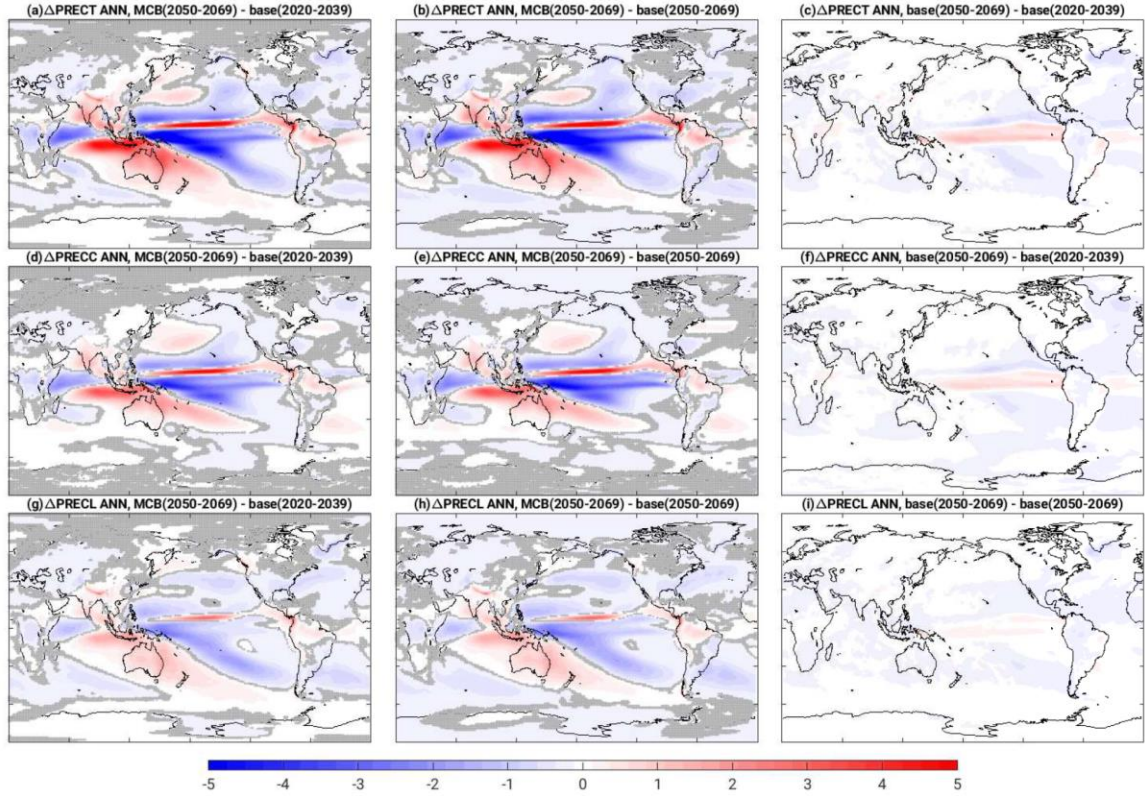
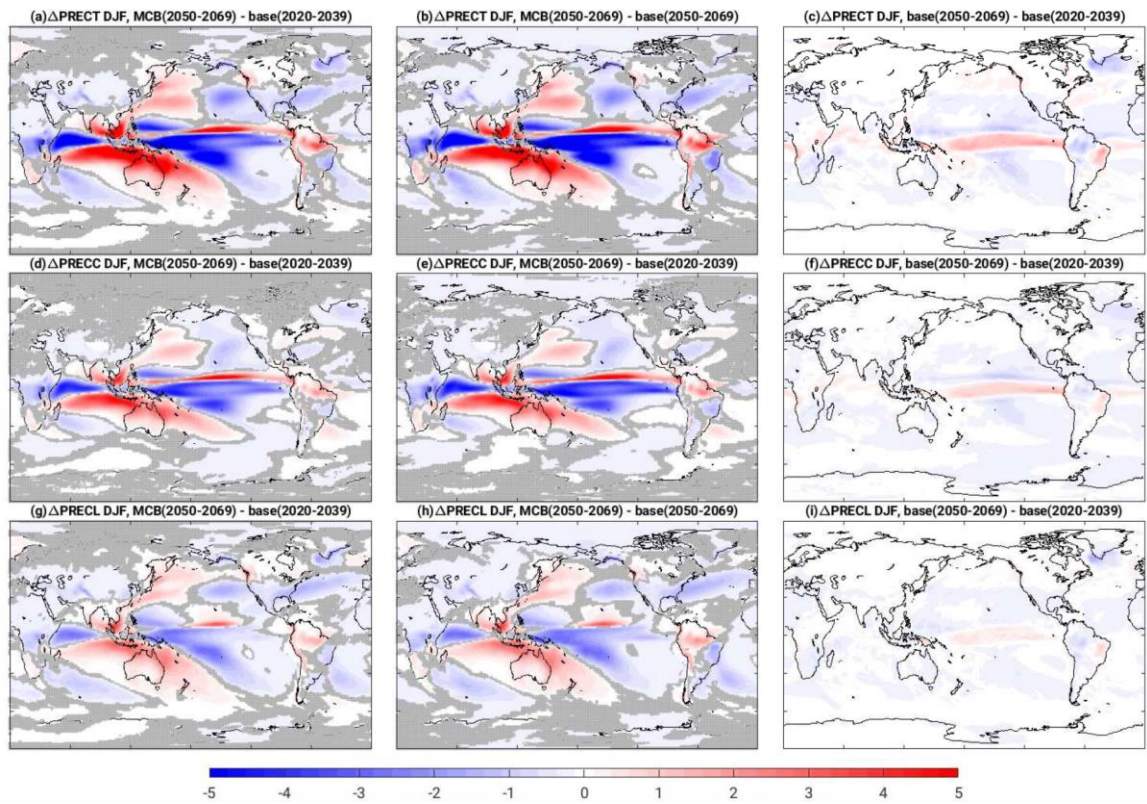


**Figure 8:** Difference in annual precipitation in mm/day between: 1) the ensemble mean of MCB over 5% ocean surface between 2050 and 2069 against the control ensemble mean between 2020 and 2039 (a,d,g), 2) the ensemble mean of MCB over 5% ocean surface between 2050 and 2069 against the control ensemble mean between 2050 and 2069 (b,e,h), and 3) the ensemble mean of the baseline model between 2050 and 2069 against the ensemble mean of the baseline model between 2020 and 2039 (c,f,i). Top panels are for total precipitation (PRECT), middle panels are for convective precipitation (PRECC), and the bottom panels are for stratiform precipitation (PRECL). Differences under the 95% significance level are marked in gray dots.



795  
796  
797



798  
799  
800  
801  
802  
803  
804  
805

**Figure 9:** Similar as Fig. 8 but for precipitation difference in boreal winter (DJF).

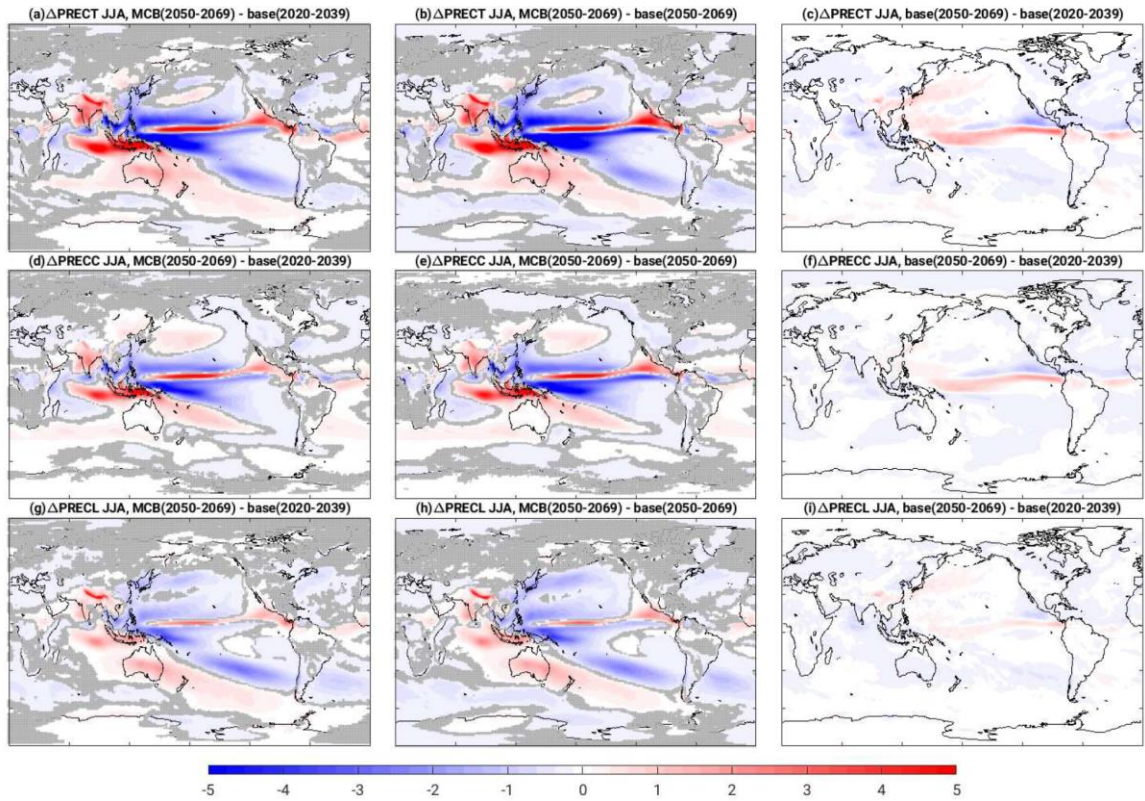


**Figure 10:** Similar as Fig. 8 but for precipitation difference in boreal summer (JJA).

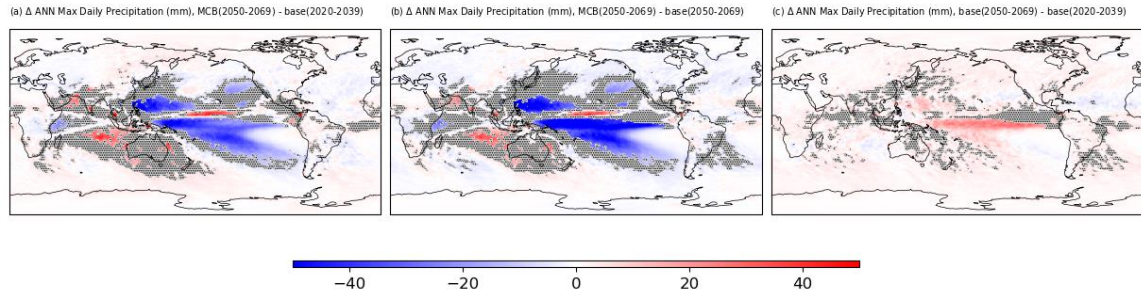


**Figure 11:** Difference in annual maximum daily precipitation between: 1) the ensemble mean of MCB over 5% ocean surface between 2050 and 2069 against the control ensemble mean between 2020 and 2039 (a), 2) the ensemble mean of MCB over 5% ocean surface between 2050 and 2069 against the control ensemble mean between 2050 and 2069 (b), and 3) the ensemble mean of the baseline model between 2050 and 2069 against the ensemble mean of the baseline model between 2020 and 2039 (c). Differences under the 95% significance level are marked in gray dots.



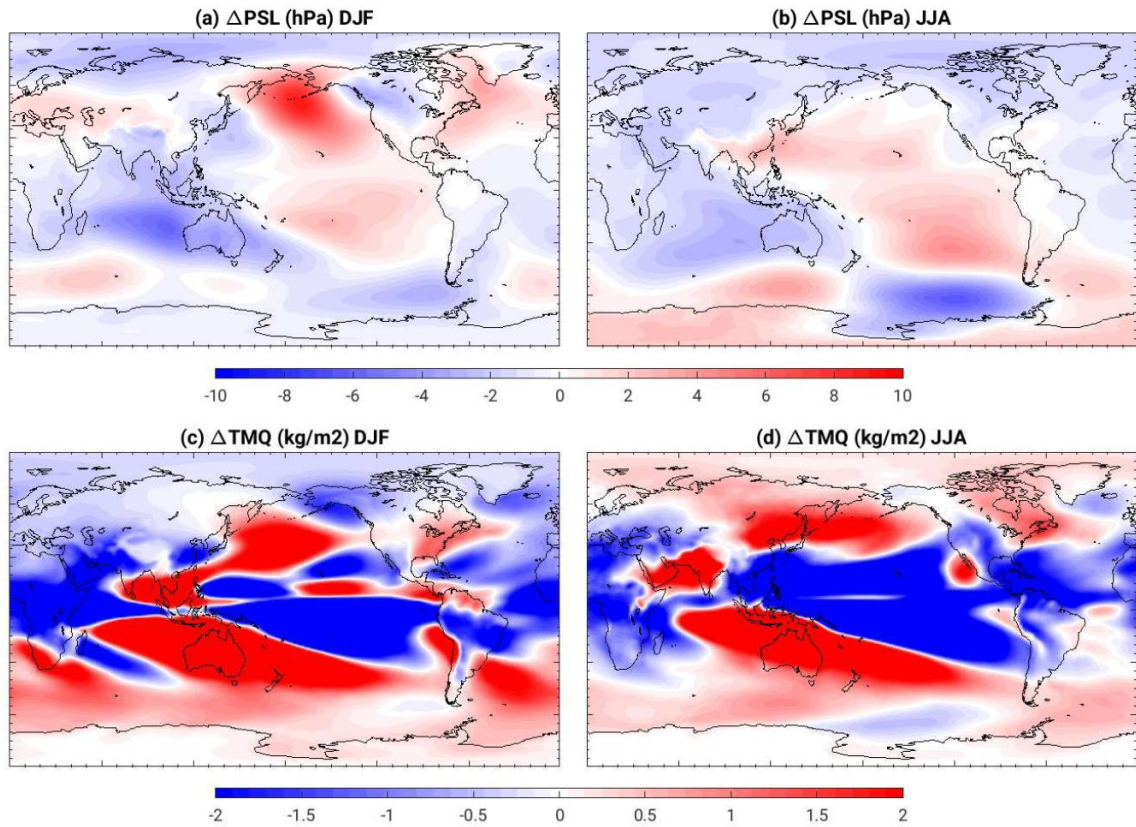


**Fig. 12:** Differences between the MCB ensemble mean between 2050 and 2069 and the control ensemble between 2020 and 2039: (a) sea-level pressure in DJF, (b) sea-level pressure in JJA, (c) total precipitable water in DJF, and (d) total precipitable water in JJA.



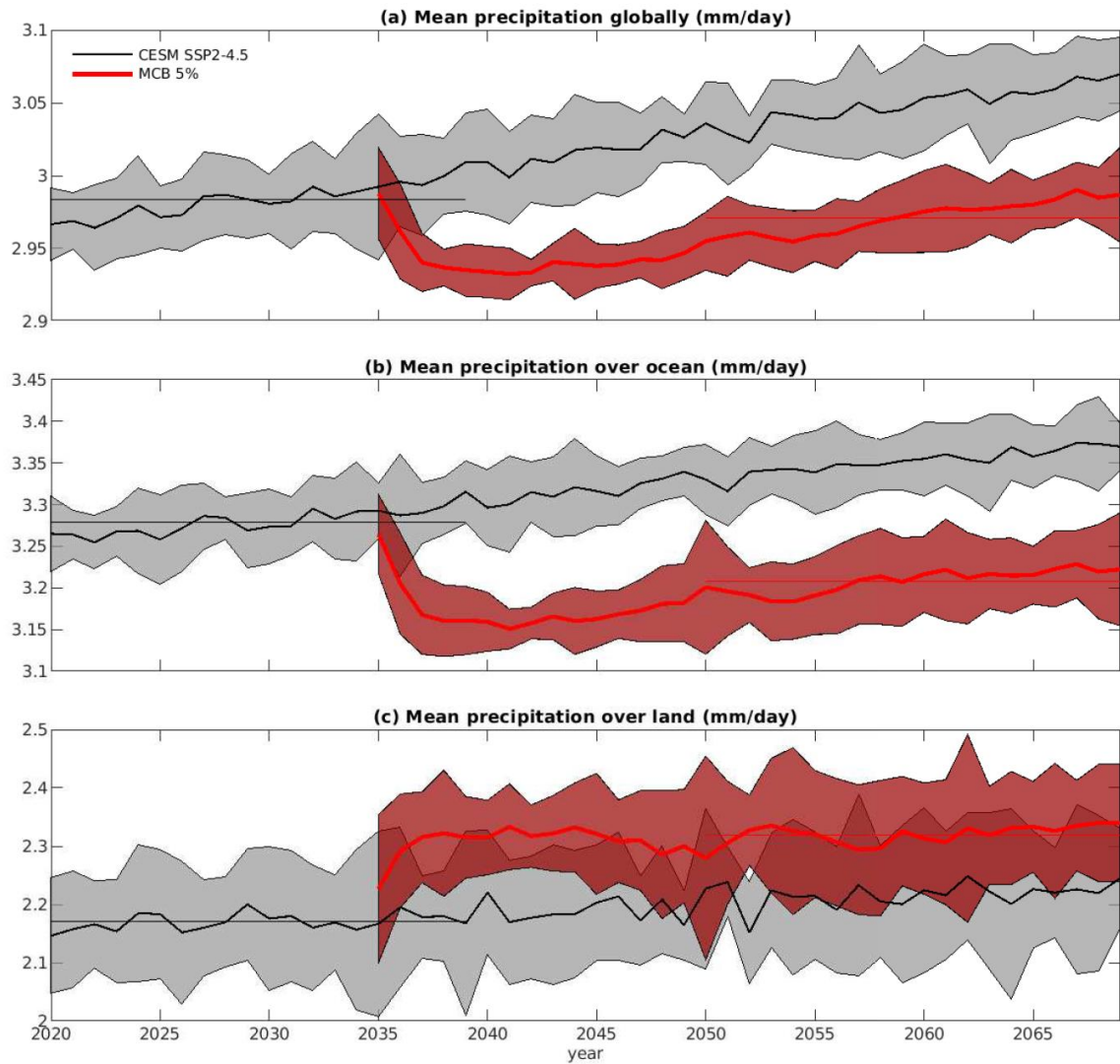


**Figure 13:** Time series of ensemble mean (thick lines) and spread (two standard deviations) of precipitation: (a) globally, (b) over ocean, and (c) over land. Control ensemble simulations are in black and ensemble simulation with MCB over 5% ocean surface are in red. Average between 2020 and 2039 from the control ensemble mean is in a thin black line, and average between 2050 and 2069 from the MCB ensemble mean is in a thin red line.

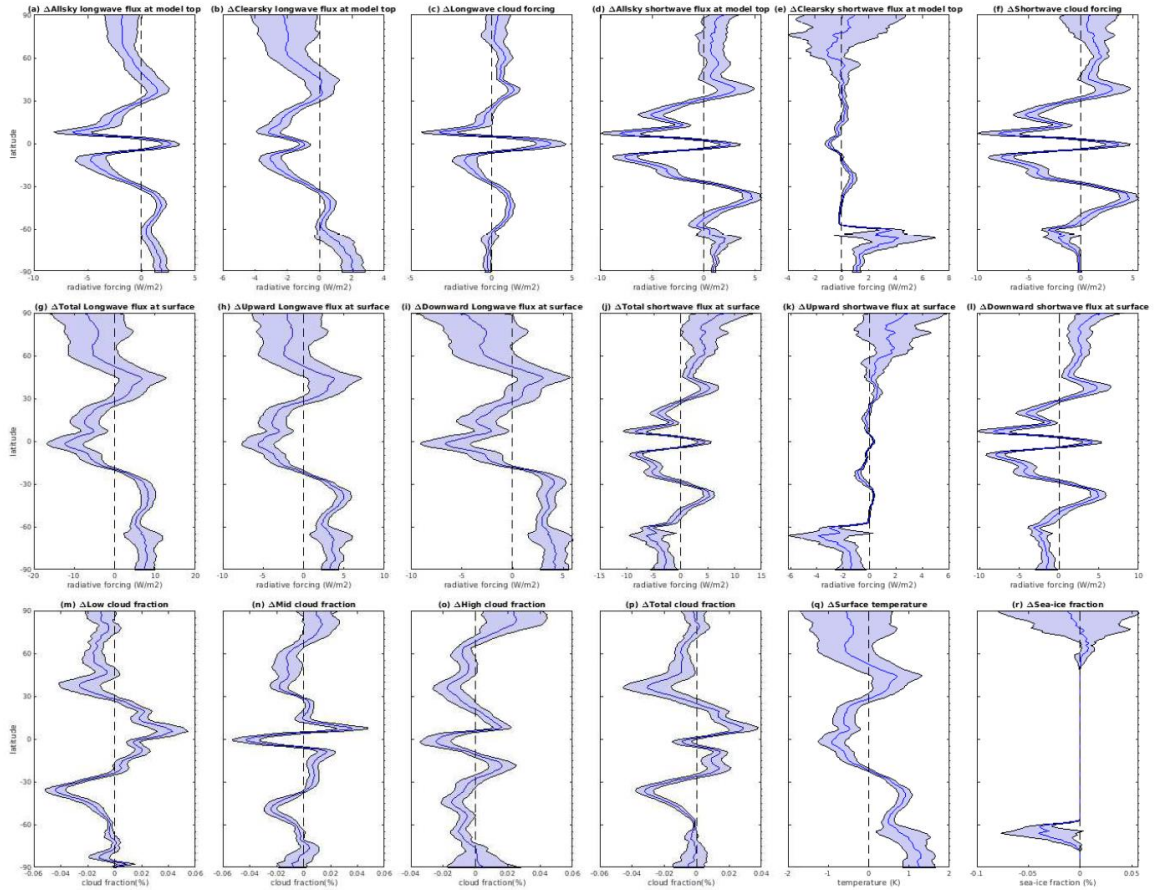


**Figure 14:** Ensemble mean difference and ensemble spread (two standard deviations) of zonal mean between the MCB (2050-2069) and control (2020-2039) ensemble simulations: (a) all-sky longwave flux at model top, (b) clear-sky longwave flux at model top, (c) longwave cloud forcing, (d) all-sky shortwave flux at model top, (e) clear-sky shortwave flux at model top, (f) shortwave cloud forcing, (g) total longwave flux at surface, (h) upward longwave flux at surface, (i) downward longwave flux at surface, (j) total shortwave flux at surface, (k) upward shortwave flux at surface, (l) downward shortwave flux, (m) low cloud fraction, (n) mid cloud fraction, (o) high cloud fraction, (p) total cloud fraction, (q) surface temperature, and (r) sea-ice fraction.